DOI: 10.1002/mrm.29864

RESEARCH ARTICLE

Magnetic Resonance in Medicine

Computational methods for the estimation of ideal current patterns in realistic human models

Ilias I. Giannakopoulos¹ | Ioannis P. Georgakis² | Daniel K. Sodickson^{1,3} Riccardo Lattanzi^{1,3}

¹The Bernard and Irene Schwartz Center for Biomedical Imaging, Department of Radiology, New York University Grossman School of Medicine, New York, New York, USA

²R&D Department, Corsmed, Stockholm, Sweden

³Center for Advanced Imaging Innovation and Research (CAI2R), Department of Radiology, New York University Grossman School of Medicine. New York, New York, USA

Correspondence

Ilias I. Giannakopoulos, Bernard and Irene Schwartz Center for Biomedical Imaging, Department of Radiology, New York University Grossman School of Medicine, New York, NY 10016, USA.

ilias.giannakopoulos@nyulangone.org

Funding information

NIH, Grant/Award Numbers: P41 EB017183, R01 EB024536

Abstract

Purpose: To introduce a method for the estimation of the ideal current patterns (ICP) that yield optimal signal-to-noise ratio (SNR) for realistic heterogeneous tissue models in MRI.

Theory and Methods: The ICP were calculated for different surfaces that resembled typical radiofrequency (RF) coil formers. We constructed numerical electromagnetic (EM) bases to accurately represent EM fields generated by RF current sources located on the current-bearing surfaces. Using these fields as excitations, we solved the volume integral equation and computed the EM fields in the sample. The fields were appropriately weighted to calculate the optimal SNR and the corresponding ICP. We demonstrated how to qualitatively use ICP to guide the design of a coil array to maximize SNR inside a head model.

Results: In agreement with previous analytic work, ICP formed large distributed loops for voxels in the middle of the sample and alternated between a single loop and a figure-eight shape for a voxel 3-cm deep in the sample's cortex. For the latter voxel, a surface quadrature loop array inspired by the shape of the ICP reached 87.5% of the optimal SNR at 3T, whereas a single loop placed above the voxel reached only 55.7% of the optimal SNR. At 7T, the performance of the two designs decreased to 79.7% and 49.8%, respectively, suggesting that loops could be suboptimal at ultra-high field MRI.

Conclusion: ICP can be calculated for human tissue models, potentially guiding the design of application-specific RF coil arrays.

KEYWORDS

ideal current patterns, integral equation methods, MRI, radiofrequency coils, ultimate intrinsic signal-to-noise ratio

1 INTRODUCTION

Ultra-high field (UHF) MR scanners can provide images with high signal-to-noise ratio (SNR) and spatiotemporal resolution. However, traditional radiofrequency (RF) coil

designs are suboptimal at UHF MRI, especially for body applications, and it was shown that denser arrays are needed to improve SNR compared to 1.5 and 3 tesla.²⁻⁴ For example, receive coil arrays with a up to 128 elements have been proposed for brain imaging at UHF.⁵⁻⁷ As the number

© 2023 International Society for Magnetic Resonance in Medicine

of RF coil elements increases, so does the prototyping cost of the array. For this reason, electromagnetic (EM) simulations⁸⁻¹¹ are often used to optimize coil designs before building prototypes. However, despite the use of parallel computing¹² and GPU programming,¹³ these simulations remain time consuming, which makes a thorough optimization of complex designs challenging.¹⁴⁻¹⁶

It was shown that ideal current patterns (ICP)2,17,18 can provide valuable physical insight to guide a tentative initial coil design, which can then be optimized more effectively in simulation. ICP confirmed the near optimality of traditional coil designs for low-field MRI but suggested that novel designs might be needed to approach the ultimate intrinsic performance at UHF.^{2,4} For example, ICP results inspired the use of electric dipoles, traditionally discounted because they were considered too lossy for MRI, for UHF head and body imaging. 19-22 Initial work on ICP was based on analytical methods, so it was limited to homogeneous spherical and cylindrical geometries.^{2,23} More recent work²⁴ employed EM bases comprising vector spherical harmonics on spherical or cylindrical shells² to determine the optimal SNR in heterogeneous head models. However, this approach is limited to spherical and cylindrical surface shells compatible with the vector spherical harmonics basis, which prevents investigating other more realistic coil formers as basis support to study ICP. Finally, another recent study suggested that the shape of the ICP depends mainly on the topology of the current-bearing surface, rather than the geometry of the sample. 18 In order to confirm such a hypothesis, and also to provide a practical tool for RF coil design and performance assessment, in this work, we introduce a method to calculate ICP associated with optimal SNR in realistic heterogeneous human head models, using volume²⁵ and volume-surface¹⁰ integral equation (VIE, VSIE) methods. Numerical methods to calculate the optimal SNR in heterogeneous head models were proposed in previous studies, 26,27 whereas this work focuses on deriving the corresponding ICP. A preliminary version of this work was presented at the 2019 meeting of the International Society for Magnetic Resonance in Medicine.²⁸

2 | THEORY

2.1 | Volume integral equation

The Galerkin²⁹ discretized current-based VIE^{25,30-32} can approximate the electric polarization currents $\mathbf{j}_b \in \mathbb{C}^{qn \times 1}$ in tissue over a uniform grid of n voxels, as a polynomial of q components per voxel. The equation has the following form:

$$(\mathbf{M}_{e_r}\mathbf{G} - \mathbf{M}_{\chi_e}\mathbf{N})\mathbf{j}_{b} = c_e \mathbf{M}_{\chi_e} \mathbf{e}_{inc}. \tag{1}$$

Here $\mathbf{M}_{\epsilon_r}, \mathbf{M}_{\chi_e} \in \mathbb{C}^{qn \times qn}$ are diagonal matrices whose entries are equal to the complex-valued permittivity and electric susceptibility, respectively, associated with each voxel. $c_e = \mathrm{i}\omega\epsilon_0$, where i is the imaginary unit, ω is the angular frequency, and ϵ_0 is the permittivity of vacuum. $\mathbf{G} \in \mathbb{C}^{qn \times qn}$ is the Grammian, $\mathbf{N} \in \mathbb{C}^{qn \times qn}$ is the discretized version of the dyadic Green's function operator that maps volumetric electric currents to electric fields, 33,34 and $\mathbf{e}_{\mathrm{inc}} \in \mathbb{C}^{qn \times 1}$ is the excitation or incident electric field from an external source. The electric field $\mathbf{e} \in \mathbb{C}^{qn \times 1}$ and magnetic field $\mathbf{h} \in \mathbb{C}^{qn \times 1}$ in the sample can be computed as follows:

$$\mathbf{e} = \mathbf{G}^{-1} \left(\frac{1}{c_e} (\mathbf{N} - \mathbf{I}) \mathbf{j}_b + \mathbf{e}_{inc} \right),$$

$$\mathbf{h} = \mathbf{G}^{-1} \left(\mathbf{K} \mathbf{j}_b + \mathbf{h}_{inc} \right),$$
(2)

where $\mathbf{h}_{\text{inc}} \in \mathbb{C}^{qn \times 1}$ is the incident magnetic field from an external source and $\mathbf{K} \in \mathbb{C}^{qn \times qn}$ is the discretized version of the dyadic Green's function operator that maps volumetric electric currents to magnetic fields. 33,34

2.2 | Volume-surface integral equation

In an MRI setup, the external source is a transmit RF coil, which delivers EM fields to the tissue-sample. Therefore, given a vector of electric coil currents $\mathbf{j}_c \in \mathbb{C}^{m \times 1}$ defined for each of the m discretization triangular elements of the coil, one can compute the incident fields as follows:

$$\mathbf{e}_{\text{inc}} = \mathbf{Z}_{\text{cb}}^{\mathcal{N}} \mathbf{j}_{\text{c}}, \quad \mathbf{h}_{\text{inc}} = \mathbf{Z}_{\text{cb}}^{\mathcal{K}} \mathbf{j}_{\text{c}}.$$
 (3)

 $\mathbf{Z}_{\mathrm{cb}}^{\mathcal{N}}, \mathbf{Z}_{\mathrm{cb}}^{\mathcal{K}} \in \mathbb{C}^{qn \times m}$ are the discretized dyadic Green's function operators that map surface electric currents to electric and magnetic fields, respectively. The electric coil currents can be computed simultaneously with the body polarization currents through the solution of the VSIE as in. 35,36

2.3 | Optimal SNR

The intrinsic SNR at a position of interest \mathbf{r}_0 accounts only for the intrinsic thermal losses due to the conductive sample and can be expressed according to³⁷ as:

$$SNR(\mathbf{r}_0) = \frac{\omega M_0 \mathbf{B}_1^{(-)}(\mathbf{r}_0)}{\sqrt{4k_B T \iiint_{V'} \left[\sigma_e(\mathbf{r}')|\mathbf{e}(\mathbf{r}')|^2\right] d^3 \mathbf{r}'}}.$$
 (4)

Here, $\mathbf{r}' \in \mathbb{R}^{n \times 3}$ is the position vector, ω is the angular operating frequency, M_0 is the equilibrium magnetization,

 $\mathbf{B}_{\mathbf{1}}^{(-)} \in \mathbb{C}^{n \times 1} (= \mathbf{h}_{x} - i \mathbf{h}_{y})$ is the receive coil sensitivity, k_{B} is the Boltzmann's constant, $\sigma_e \in \mathbb{R}^{n \times 1}$ is electric conductivity of the sample, and T is the average temperature of the sample. The triple integration in the denominator of (4) is over the entire volume (V') of the sample.

In the case of coil arrays with p elements, the equation (4) can be written as:

$$SNR(\mathbf{r}_0) = \frac{\omega M_0 \mathbf{B}_1^{(-)}(\mathbf{r}_0) \mathbf{w}}{\sqrt{4k_B T \mathbf{w}^H \mathbf{\Psi} \mathbf{w}}},$$
 (5)

where $\mathbf{B}_{\mathbf{1}}^{(-)}$ is now a matrix $\in \mathbb{C}^{n \times p}$ whose number of columns corresponds to the number of coils and $\mathbf{w} \in \mathbb{C}^{p \times 1}$ are the weights used to combine individual coils contributions. The elements of the noise covariance matrix³⁸ $\Psi \in$ $\mathbb{R}^{p \times p}$ that accounts for the intrinsic thermal losses due to the sample's conductivity can be computed for each coil pair p_1, p_2 as:

$$\mathbf{\Psi}_{p_1,p_2} = \iiint_{V'} \left[\sigma_e(\mathbf{r}') \mathbf{e}_{p_2}^{\mathrm{H}}(\mathbf{r}') \mathbf{e}_{p_1}(\mathbf{r}') \right] d\mathbf{r}'^3.$$
 (6)

The coil combination weights that yield the optimal SNR are given by ^{39,40}:

$$\mathbf{w} = \left[\mathbf{B}_{1}^{(-)H}(\mathbf{r}_{0}) \mathbf{\Psi}^{-1} \mathbf{B}_{1}^{(-)}(\mathbf{r}_{0}) \right]^{-1} \mathbf{B}_{1}^{(-)H}(\mathbf{r}_{0}) \mathbf{\Psi}^{-1}. \tag{7}$$

By substituting (6) and (7) into (5), the optimal SNR at \mathbf{r}_0^{41} can be expressed as

$$SNR_{opt}(\mathbf{r}_0) = \frac{\omega M_0}{\sqrt{4k_B T \Big[\mathbf{B}_1^{(-)}(\mathbf{r}_0)\mathbf{\Psi}^{-1}\mathbf{B}_1^{(-)H}(\mathbf{r}_0)\Big]^{-1}}}.$$
 (8)

2.4 Ultimate intrinsic SNR and ICP

Given Equation (3) we can construct a basis of incident EM fields by assembling the discretized Green's function operators $\mathbf{Z}_{cb}^{\mathcal{N}}$ and $\mathbf{Z}_{cb}^{\mathcal{R}}$ between a sample and a closed surface that surrounds it. The surface must be located outside the sample to obey the Huygens-Fresnel principle, 42 so that all possible EM field distributions within the sample generated from RF sources external to the surface can be accurately represented.

 $\mathbf{Z}_{ch}^{\mathcal{K}}$ can be compressed and orthogonalized using a truncated singular value decomposition (SVD)²⁷ as follows:

$$\mathbf{Z}_{cb}^{\mathcal{K}} \approx \mathbf{U}_{\mathcal{K}} \mathbf{\Sigma}_{\mathcal{K}} \mathbf{V}_{\mathcal{K}}^{H}$$

$$\mathbf{U}_{\mathcal{N}} = \mathbf{Z}_{cb}^{\mathcal{N}} \mathbf{V}_{\mathcal{K}} \mathbf{\Sigma}_{\mathcal{K}}^{-1}.$$
(9)

Here, $\mathbf{U}_{\mathcal{N}}$ and $\mathbf{U}_{\mathcal{K}}$ are bases of electric and magnetic incident fields consistent with electrodynamics principles.⁴³ $\Sigma_{\mathcal{K}}$ is a diagonal matrix containing the singular values of $\mathbf{Z}_{ch}^{\mathcal{K}}$ up to the predefined tolerance of the SVD. The columns of $\mathbf{V}_{\mathcal{K}}$ are the right singular vectors of $\mathbf{Z}_{ch}^{\mathcal{K}}$.

After the two bases are constructed, the VIE (1) can be rapidly solved, ^{13,44} using each column of $\mathbf{U}_{\mathcal{N}}$, $\mathbf{U}_{\mathcal{K}}$ as an excitation, to compute an EM basis of e and h fields in the sample. The combination weights (7) and the associated optimal SNR (8) can be computed at any voxel of interest in postprocessing using the **e** and **h** fields.

As we increase the number of columns of $\mathbf{U}_{\mathcal{N}}$ and $\mathbf{U}_{\mathcal{K}}$ we include additional excitation modes in the EM basis. As the number of modes increases, the value of the optimal SNR (8) will converge to a maximum bounding value, which depends on the geometry of the surface where the sources are defined. In particular, if the surface is closed and fully surrounds the sample, then the SNR will converge to its ultimate intrinsic upper bound called UISNR, ^{23,40,41,45} which is the theoretical maximum limit of achievable SNR for the particular sample. By combining the excitations using the weights in (7) we can approximate the incident fields that lead to such maximum SNR values at \mathbf{r}_0 as $\mathbf{e}_{inc} = \mathbf{U}_{\mathcal{N}} \mathbf{w}$ and $\mathbf{h}_{inc} = \mathbf{U}_{\mathcal{K}} \mathbf{w}$. Finally, the ICP on the current-bearing surface of choice can be computed based on (3) and (9) as

$$\mathbf{j}_{ideal}(\mathbf{r}) \approx \mathbf{V}_{\mathcal{K}} \mathbf{\Sigma}_{\mathcal{K}}^{-1} \mathbf{w}.$$
 (10)

Note that Equation (10) refers to the complex spatial pattern of ICP at time t = 0. In order to visualize the evolution of the ICP in time we can perform the following spatiotemporal conversion:

$$\hat{\mathbf{j}}_{\text{ideal}}(\mathbf{r}, t) = \text{Re}(\hat{\mathbf{j}}_{\text{ideal}}(\mathbf{r})e^{i\omega t}),$$
 (11)

where i is the imaginary unit and \mathbf{r} is the position in the current-bearing surface. Note that the ICP yield the UISNR only if defined on a closed surface surrounding the sample, as in Figure 1A. For all other current-bearing surfaces in Figure 1, the ICP correspond to the largest SNR theoretically achievable by any coil defined on such formers.

METHODS

3.1 Numerical samples

We calculated ICP associated with optimal SNR inside the head of the realistic Duke human model from the virtual family. 46 The distribution of relative permittivity and electric conductivity inside the head model at 7T is shown in

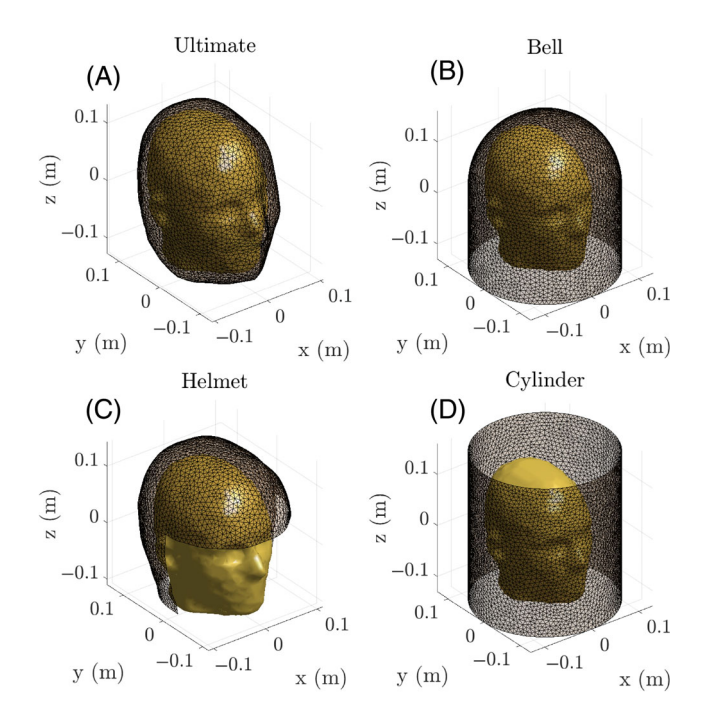


FIGURE 1 Geometry of the ultimate (A), the bell-shaped (B), the helmet-shaped (C), the cylindrical (D), and the spherical (E) current-bearing surfaces. The surface surrounded a realistic head model (Duke), with the ultimate one being the only closed surface and having the minimum distance from the sample.

Figure S1. The computational domain enclosing the head model was $18.5 \times 23 \times 22.5$ cm³ and was discretized over a uniform grid of 5 mm³ voxel resolution, corresponding to $38 \times 47 \times 46$ voxels.

For validation, we qualitatively compared the ICP calculated with our proposed numerical method and with an analytic method² for the case of a uniform spherical sample with relative permittivity 50 and conductivity 0.4 S/m (resembling average brain electrical properties). The sphere had a 10-cm radius and was discretized over a uniform grid of 5 mm³ voxel resolution.

3.2 | Currents-bearing surfaces

We generated an ultimate basis that fully captures the UISNR in Duke's head based on the Huygens-Fresnel principle.⁴² In particular, we defined our ultimate EM basis (9) on a Hugyens' surface fully surrounding the head⁴³ (Figure 1A), which we constructed by expanding the isosurface of the sample by approximately 2 cm. The ultimate basis was discretized with 7254 triangular elements. We also modeled the surface of three realistic receive RF coil array formers and generated their respective EM bases. The first former⁶ resembled a bell structure (Figure 1B) with height 29 cm and radius 13 cm.

8870 triangular elements were used for its discretization. The second former^{47,48} resembled a helmet-shaped surface (Figure 1C). The helmet was constructed by expanding the isosurface of the Duke's head by approximately 3 cm and forcing a symmetry along the y-axis. 5212 triangular elements were needed for its discretization. The third former resembled what is normally used for birdcage⁴⁹ and other volume coil designs.⁵⁰ We modeled it as an open cylindrical surface (Figure 1D) of length 29 cm and radius 13 cm, using 8824 triangular elements for discretization.

For the case of the spherical sample, since the analytical solution requires an enclosing spherical surface concentric with the sample, we designed a spherical shell (Figure S2) of radius 13 cm, discretized it with 8464 triangular elements, and generated the EM basis. We used the same average triangle edge size of 8 mm for the discretization of all current-bearing surfaces, and all studied MR frequencies.

3.3 | RF coil models

We modeled single loops of three radii (4.15 cm, 3.1125 cm, and 2.075 cm) (Figure 2 top) and three corresponding surface quadrature configurations, with a loop positioned at the center of a figure-eight coil (Figure 2 bottom) and compared their SNR for different voxel positions against the corresponding UISNR. The conductor width was 0.3 cm for all cases. The coils were placed close to the helmet former (positioned on the exterior of the surface (Figure S3), and, in each case, their position was chosen based on the shape of the ICP for the voxel of interest (4.3). We used the VSIE to compute the SNR. The loops were segmented with one (1.5T, 3 T) or seven (7 T) capacitors for tuning and one capacitor connected in parallel to the feeding port for matching. We assumed ideal decoupling between the three loops of the array. The coils were discretized with elements of the same resolution as the basis surfaces, yielding 102, 88, and 72, elements per loop of radius 4.15, 3.1125, and 2.075 cm, respectively.

3.4 | Simulation settings

All simulations were performed on a server running Ubuntu 20.04.2 LTS operating system, with an Intel(R) Xeon(R) Gold 6248R CPU at 2.70GHz, 112 cores, 2 threads per core, and an NVIDIA A100 PCIe GPU with 40GB of memory. We used our custom integral equation methods which borrow some routines from the open-source software MARIE.¹⁰ The VIE was solved with the aid of the higher-order singular value decomposition (HOSVD),¹³ and the VSIE with the aid of the precorrected fast Fourier

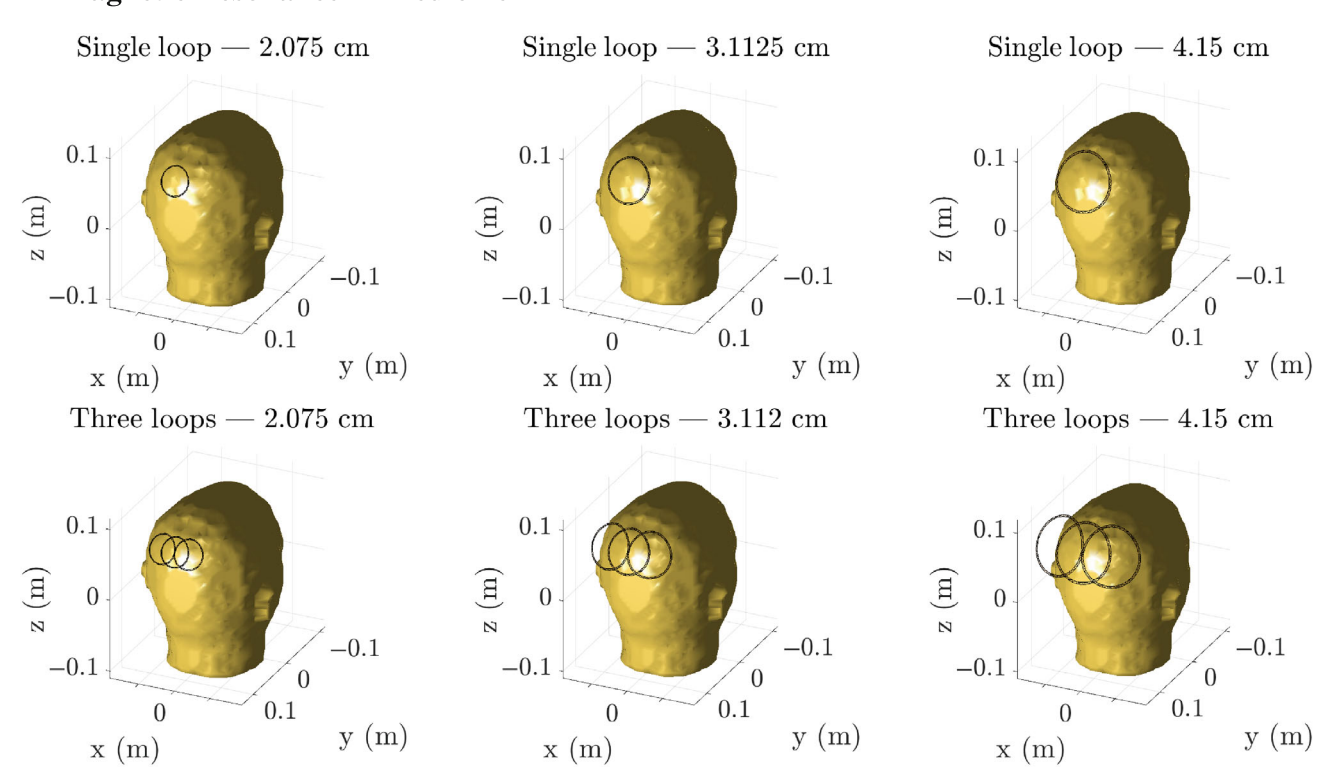


FIGURE 2 Geometry of the single loops (top) and three-element arrays (bottom) relative to the head model. The loop radius is decreasing from left to right.

transform.⁵¹ Both integral equations were solved with the generalized minimal residual algorithm (GMRES)52 and tolerance 1e - 5. HOSVD's tolerance was set to 1e - 7. We used a truncated SVD of 1e - 3 tolerance to construct the EM bases for the heterogeneous samples and 1e-2 for the homogeneous ones. In order to achieve high accuracy for the calculated fields,³⁴ for the simulations involving heterogeneous samples we used first-order polynomials to approximate the polarization currents, thus, 12 unknowns per voxel. For the simulations that involved homogeneous samples, we used zeroth-order polynomials (3 unknowns per voxel). The coil models were tuned and matched using the optimization method presented in Reference 53. Finally, the surface currents were approximated over the triangular discretization using the well-established Rao-Wilton-Glisson (RWG) basis functions.⁵⁴

4 | RESULTS

4.1 Validation against the analytic solution

Figure 3 compares the numerical ICP, obtained with our proposed method, and analytical ICP, obtained with a complete basis of spherical harmonics,² for the central voxel of a tissue-mimicking dielectric sphere.

The simulations were performed at 7 tesla Larmor frequency. The ICP look the same in both cases, forming two large distributed current loops that precess around the z-axis. Figures S4 and S5 compare the same simulation for 1.5 and 3 T frequencies, and present high similarity between the analytic and the numerical method as well.

4.2 | Effect of former topology on the optimal SNR

In Figure 4, we compare the spatial distribution of the optimal SNR at 7 T for the central planes and additional representative axial plane of Duke for the four different formers: ultimate, bell, helmet, and cylinder. The number of basis vectors (modes) to achieve a 1e-3 singular value drop in the SVD of (9) was not equal for all cases (Figure S6) and depended on the geometry of the basis former. In particular, 3149, 761, 855, and 585 modes were needed for the ultimate, bell, helmet, and cylindrical bases, respectively, to reach the desired tolerance. The time footprint to compute the SVD in (9) was approximately 38, 47, 21, and 51 min, while the weights in (7) were computed in approximately 520, 125, 140, and 95 min for the ultimate, bell, helmet, and cylindrical formers, respectively.

In Figure 5, we compare the slope of the optimal SNR for the four formers as the number of basis modes

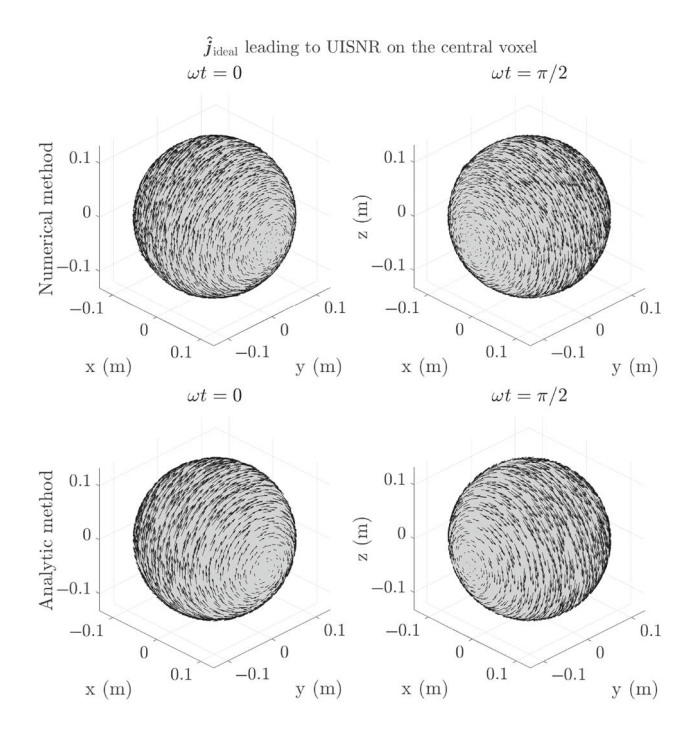


FIGURE 3 Ideal current patterns (ICP) on the spherical shell computed numerically with the proposed approach (top) and analytically using a complete basis of spherical harmonics (bottom) for a voxel located at the center of a homogeneous dielectric sphere and 7 T. Both current patterns form two large distributed current loops precessing around the sphere. The first row corresponds to ICP at $\omega t = 0$, while the second row presents them after a $\omega t = \pi/2$ time delay. The spherical sample is omitted from the figure, and instead, the surface shell is shown in gray for visual aid.

increases. The convergence (slope approaching zero) is shown for four voxels in the central sagittal slice of Duke. To generate the plots in Figure 5, we evaluated the optimal SNR for each basis by increasing the number of modes until reaching the 1e-3 singular drop in the SVD of (9). The largest SNR associated with the realistic coil formers is presented as a percentage of the UISNR in Table 1 for the four voxels of interest.

4.3 | Simulated ICP

Figure 6 shows a temporal snapshot of the ICP that yielded optimal SNR for the intermediate voxel at 7 T (Results for the bottom, middle, and top voxels are presented in Figures S7, S8, and S9, respectively. For all current-bearing surfaces, the ICP formed two distributed figure-eight loops. Smaller loops formed by currents of lower intensity were present for the cylindrical basis. In Figure 7, we present the time evolution (four time-points) of the ICP for the helmet former for 1.5, 3, and 7 T. As expected in surface quadrature reception, 2 the dominant component of

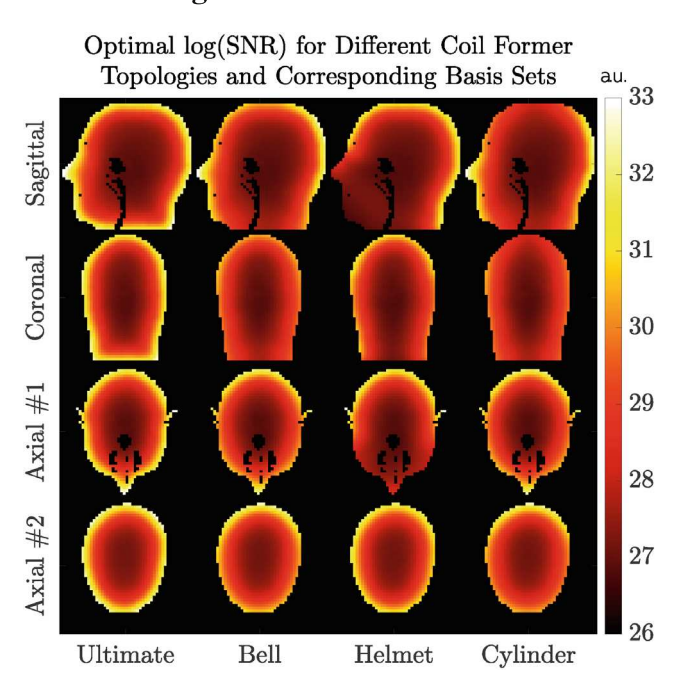


FIGURE 4 Comparison of the ultimate intrinsic signal-to-noise ratio (SNR) with the largest SNR achieved with the various formers. Maps are in logarithmic scale and arbitrary units for the central sections (Sagittal, Coronal, and Axial #1) of the head model and an additional representative axial slice (Axial #2). Note that in most regions, the SNR is almost identical for all cases.

the ICP alternated between a butterfly configuration and a single-loop every $\pi/(2\omega)$ and shift direction every π/ω .

4.4 | RF coil simulations

Table 2 presents the percentage of the UISNR at the intermediate voxel of the head model for 1.5, 3, and 7 T Larmor frequency and three loop radii, for all coil configurations. The percentage drops for larger loop radii and larger field strengths. For all cases, the absolute performance of the surface quadrature array inspired by the ICP in Figure 7 was approximately 1.6 times larger than the single loop performance for the intermediate voxel. Absolute performance maps for all coil configurations are presented for the central sagittal slice of Duke in Figure 8.

5 | DISCUSSION

The aim of this work was to introduce a new method to calculate the ICP that yield optimal SNR in heterogeneous realistic anatomical models. The use of numerical EM bases²⁷ allowed the computation of a set of incident EM fields generated from electric currents sources defined on a surface surrounding the sample. We used a fast¹³

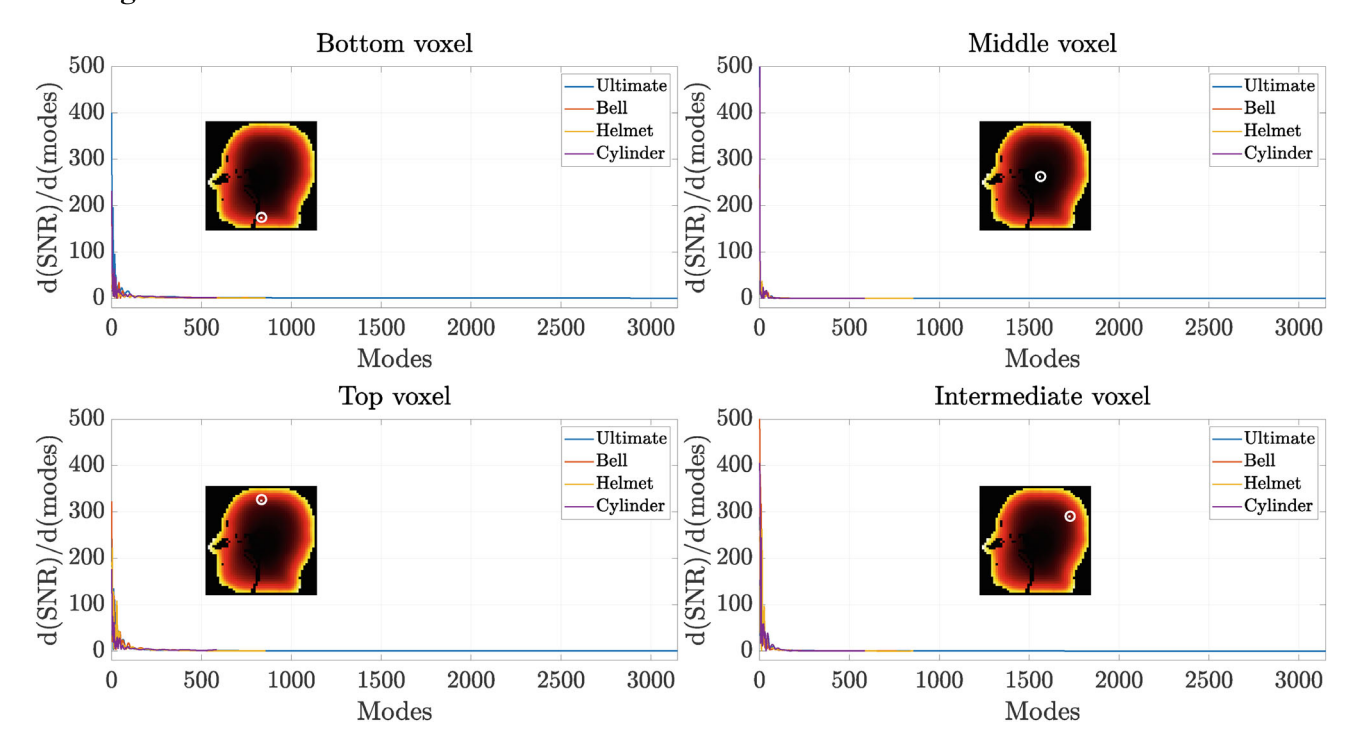


FIGURE 5 Convergence of the signal-to-noise ratio (SNR) expressed as its numerical derivative with respect to the number of modes for 7 T MR frequency. The SNR grew rapidly at the beginning and converged monotonically to the optimal value for all formers and voxel locations. The oscillations at the beginning of the curves reflect changes in the rate of convergence. For visual clarity we present the corresponding voxel location inside the ultimate intrinsic signal-to-noise ratio map.

TABLE 1 Percentage of the ultimate intrinsic signal-tonoise ratio (SNR) achieved by the largest SNR achievable using the realistic coil formers, for the middle, top, bottom, and intermediate (3 cm deep in the sample's cortex) voxels in the head.

Coil former / Voxel	Middle	Тор	Bottom	Intermediate
Bell	98%	93%	44%	100%
Helmet	96%	97%	31%	99%
Cylinder	98%	63%	44%	99%

Note: All values are rounded to the nearest integer above its current value.

and accurate³⁴ VIE solver (1) to estimate the corresponding total electric and magnetic field inside the sample (2). The combination weights (7) that yield optimal SNR for a voxel of interest were then used also to calculate the associated ICP.

Our approach requires the setting of three tolerances for the HOSVD, GMRES, and SVD. Based on previous work on the VIE method, 30,34 a 1e-5 GMRES tolerance is expected to be enough to generate accurate results. To avoid false convergence of GMRES, its tolerance must be set at least one to two orders of magnitude lower than the tolerance of the HOSVD, otherwise erroneous numerical digits will be fitted in its solution. A lower tolerance for SVD than GMRES would result in an inaccurate

estimation of the effect of the incident fields on the sample, leading to erroneous total fields. The tolerance of the SVD determines not only the accuracy of the compressed representation of the incident EM fields but also the number of basis modes. In fact, in our numerical approach, the number of modes is essentially the rank of $\mathbf{Z}_{cb}^{\mathcal{K}}$ up to the predefined SVD tolerance, which is directly related to the distance between the discretization elements, which in our case was the distance between the triangular elements of the surface shell and the voxels of the sample. Rather than fixing the number of modes, which could have become computationally intractable, in this work, we decided to fix the SVD tolerance, which allowed us to have a fair comparison of the optimal SNR values between the different cases.

We validated the ICP calculated with our proposed numerical method against the analytical solution for a dielectric sphere. Despite the unavoidable staircase effect when discretizing a curved surface and the numerical integration errors introduced in the construction of $\mathbf{Z}_{cb}^{\mathcal{K}}$ and $\mathbf{Z}_{cb}^{\mathcal{N}}$, the ICP based on our new approach qualitatively matched the analytic ICP (Figure 3). A direct quantitative comparison between the analytical and numerical currents is not practical due to the discrete nature of the numerical currents plotted over a discretized surface, which may result in different locations compared to the

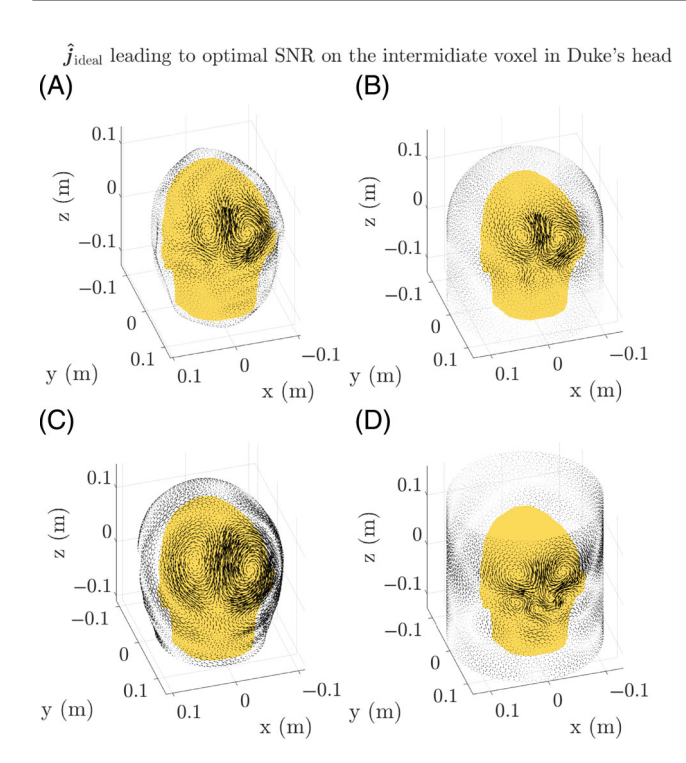


FIGURE 6 A temporal snapshot of the ideal current patterns yielding optimal signal-to-noise ratio at a voxel located in the back of the head for the (A) ultimate, (B) bell, (C) helmet, and (D) cylinder formers at 7 T.

analytically calculated currents. Nevertheless, the discrepancies between the two cases are primarily associated with the numerical error between volume integral equations and vector spherical harmonics (Mie theory), which has been extensively studied in the literature.³⁴

In addition to the ultimate surface that yielded the true UISNR (an absolute performance benchmark), we used three surfaces that resembled realistic coil formers to evaluate the shape of the ICP and the value of the associated optimal SNR with respect to the ultimate case. To construct the bases, we used a relatively high SVD tolerance (1e-3) because a lower one would lead to a large number of basis modes, resulting in possible memory overflows, or numerical instabilities in GMRES' convergence. For the ultimate basis support that tightly fitted the head model and fully enclosed it, this threshold resulted in approximately 3100 modes. For all other bases less than 860 mode were sufficient to achieve this threshold (Figure S6), which explains the truncated lines appearing in Figure 5.

For the intermediate voxel (Figure 5), the SNR converged closely to the UISNR for all surfaces. According to Table 1, for the middle voxel, the basis of the helmet former achieved a slightly lower SNR than the ultimate case. This happened because the helmet does not fully surround the sample (Figure 1), so the respective EM basis cannot fully capture all possible EM fields in contrast to the other

formers. A similar pattern was found for the cylinder basis and the top voxel since the top area of the head is not covered by the cylindrical surface. For the bottom voxel, the bell, helmet, and cylinder formers all achieved lower values than the UISNR, since they do not cover the bottom area of the sample. Overall, the SNR convergence (Figure 5) was slower for voxels placed close to the surface rather than deep inside the sample. In particular, the derivative of the SNR required more modes to reach zero for the top and bottom voxels than for the intermediate and middle voxels. This finding was in agreement with previous work that showed similar convergence trends. 40,56 Note that convergence of the UISNR at superficial locations could be more easily obtained by moving the current-bearing former farther away from the sample. In fact, this would reduce the number of modes needed for convergence. However, the shape of the ICP would change.¹⁷ Since we were interested in the shape of ICP for realistic coil formers rather than the exact value of the UISNR at every location, in this work, we chose not to increase the distance between the surface and the sample. In fact, a perfect convergence at the surface of the body is not critical to achieve qualitatively correct ICP shapes.

As in the case of spherical objects,² for a voxel in an intermediate region of the sample (3 cm deep in the sample's cortex), the ICP overall resembled a surface quadrature coil.⁵⁷ In particular, they alternated in time between a figure-eight and a single loop (Figure 7). This was the case for all formers, although the shape and size of the ICP slightly changed based on the former. This confirms the hypothesis formulated in Reference 18 that the shape of the ICP mainly depends on the topology of the former, rather than the geometry of the sample.

We designed arrays combining a loop with a figure-eight coil in Figure S3 on top of the helmet former based on the shape of the ICP in Figure 6 and compared the resulting SNR with that achieved by using just a loop. As reported also in previous work based on an analytic method,² we found that the SNR performance increased with the surface quadrature array⁵⁷ and specifically was around 1.6 times higher than for the single loop for all studied radii and Larmor frequencies. The SNR performance in the intermediate voxel decreased for loops of larger radius. In fact for an 1.5x increase in the loop's radius, starting from approximately 2 cm, the SNR dropped approximately 2%, 3%, 2% for the single loop and approximately 1%, 1.5%, and 0.5% for the three-loop configuration at 1.5, 3, and 7 T, respectively. A 2× increase in the radius led to a approximately 7%, 7%, and 5% SNR drop for the single loop and a 6%, 7%, and 5% drop for the three-loop array at 1.5, 3, and 7 T, respectively. To ensure a fair comparison between the coil SNR and the UISNR,

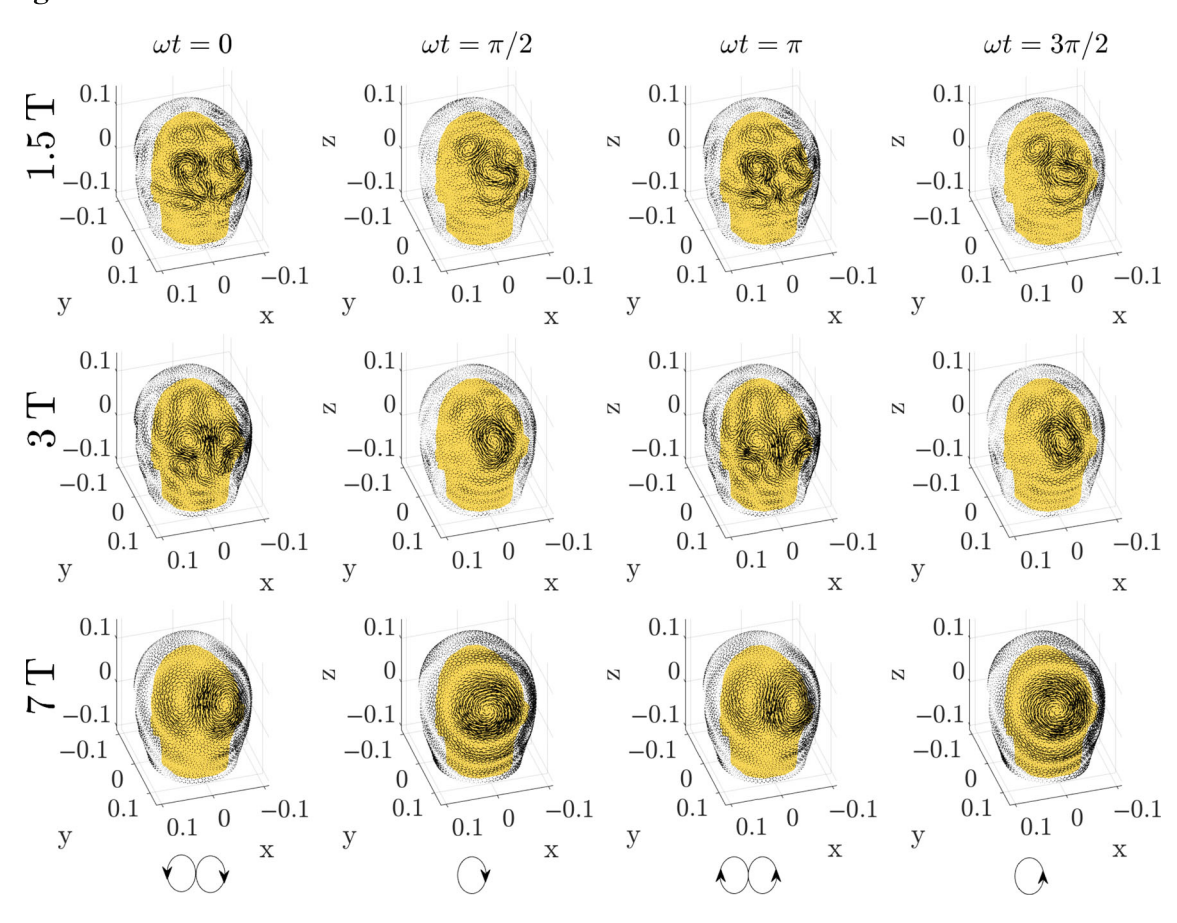


FIGURE 7 Temporal snapshots of the ideal current patterns yielding optimal signal-to-noise ratio at a voxel in the back of the head for the helmet former at 1.5, 3, and 7 T. Four time-points are shown with equal time differences $\delta(\omega t) = \pi/2$.

TABLE 2 Percentage of the ultimate intrinsic signal-to-noise ratio (SNR) achieved by the coil configurations for the intermediate voxel in the head.

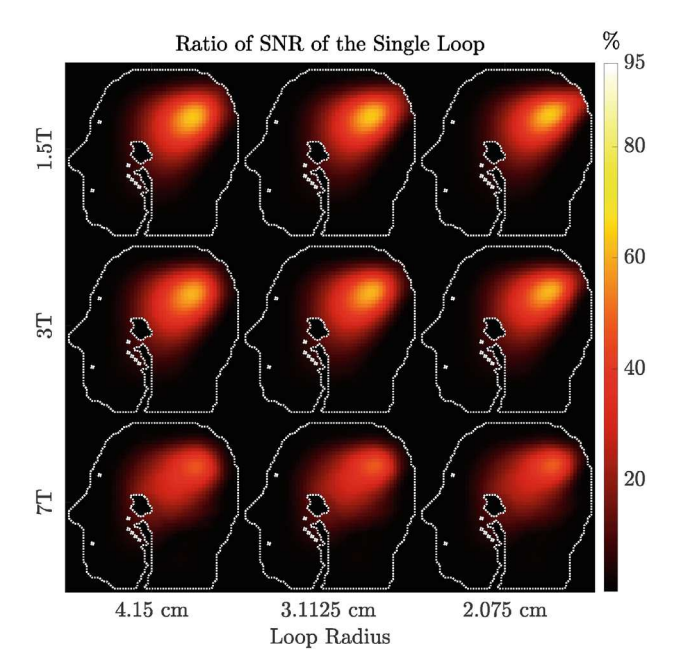
Coil configuration	Loop radius (cm)	1.5 T	3 T	7 T
Single loop	4.15	51.5%	48.4%	44.7%
	3.1125	55.6%	52.5%	47.6%
	2.075	58.7%	55.7%	49.8%
Surface Quadrature	4.15	85.1%	80.6%	75.1%
	3.1125	90.0%	85.8%	79.2%
	2.075	91.2%	87.5%	79.7%

Note: The SNR drops with higher field strengths and with larger loop radius.

we used the same resolution for the discretization mesh of the basis surface and the coil conductors, since finer or coarser meshes could lead to underestimation or overestimation of the SNR, respectively. While the radius of the loop affects SNR performance, Figure 6 shows that the ICP are complex, distributed current patterns, therefore adjusting the loop radius by qualitatively observing the ICP is not sufficient to thoroughly optimize coil design.

In fact, ICP can provide insight about the number, size, type and position of the coils, but to design a coil that closely resembles the ICP and can capture the UISNR performance would require a sophisticated coil optimization process that accounts for the coils' position, radius, and conductor width. This is beyond the scope of this paper and will be the subject of future work.

Previous approaches to calculate the UISNR in heterogeneous human models were based on expanding the EM basis using dipole clouds surrounding the object. 26,27 In these cases, the calculation of the ICP is not straightforward and requires nontrivial postprocessing steps in order to project the current patterns to the surface of interest. Here, we used RWG functions, which facilitate the visualization of the ICP, although our approach is still different than what is used in analytic methods.² In particular, we do not solve a surface integral equation to compute the coefficients that would optimally combine the RWG basis functions, but instead, we solve the VIE using external excitations and then use the RWG functions as projections of the incident fields back to the current-bearing surface. As a result, the SVD in (9) forms a nonlinear relation between the EM basis and the



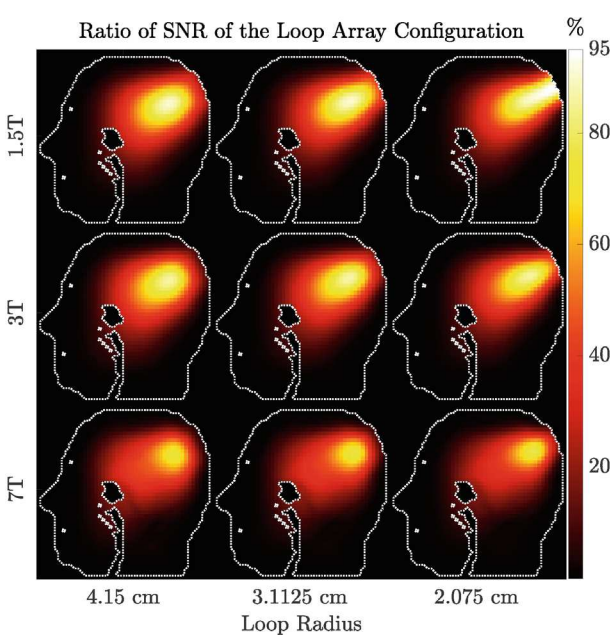


FIGURE 8 Performance maps of the single loop (top) and the three-loop array configuration (bottom), for three loop radii, in Figure 2, displaying their signal-to-noise ratio (SNR) as a percentage of the ultimate intrinsic signal-to-noise ratio for the central sagittal plane at 1.5, 3, and 7 T. The SNR performance is higher for the array and for smaller loop radii. It also decreases for all cases at higher magnetic field strengths. The dotted white line contours the area with tissue voxels.

size of the triangular elements since the RWG functions depend on the triangular element's size, which is not constant throughout the mesh. This can lead to nonsmooth current patterns (somehow evident in Figure 6) because the currents are not properly normalized based on the triangle's size. In future work, we plan to use curvilinear triangular elements and the higher order interpolatory vector basis Graglia–Wilton–Peterson. We expect that Graglia–Wilton–Peterson could allow for a better discretization of the curved surfaces, resulting in meshes with almost equal-sized elements, which would enhance the visualization of the ICP.

The computational methods presented in this work are constrained by memory limitations. In particular, the assembly of $\mathbf{Z}_{cb}^{\mathcal{N}}$ and $\mathbf{Z}_{cb}^{\mathcal{K}},$ for the basis generation in Equation (9), has a vast memory footprint, that can reach the TB range for fine voxel resolutions or low SVD tolerances. One solution could be to compress these matrices by exploiting their hidden low-rank structures. In fact, their columns could be reshaped as three-dimensional tensors (due to the three-dimensional uniform grid that was used for the discretization of the sample) that can be significantly compressed with the HOSVD. 59,60 As a result, $\mathbf{Z}_{cb}^{\mathcal{N}}$ and $\mathbf{Z}_{cb}^{\mathcal{K}}$ would be reshaped as four-dimensional tensors that can be compressed with the HOSVD or tensor train-SVD. 61,62 This approach would reduce the memory demands by thousands of times compared to the traditional SVD in (9). However, it cannot be employed directly with the method introduced in this work. In fact, to ensure the orthogonality of the incident fields inside the sample, we applied the traditional SVD only on the voxels that belong to the sample and not to the entire three-dimensional domain that encloses it. Therefore, $\mathbf{Z}_{cb}^{\mathcal{N}}$ and $\mathbf{Z}_{cb}^{\mathcal{K}}$ have an incomplete four-dimensional structure and HOSVD or tensor train-SVD are not applicable. To address this, future work will investigate the compression of such incomplete four-dimensional structures using tensor completion schemes.63

6 | CONCLUSION

We introduced a new computational method to calculate ICP associated with optimal SNR in any sample and for any current-bearing surface of interest. We demonstrated our method for the case of a heterogeneous head model, presenting ICP associated with different surfaces and showing that they can qualitatively guide coil design. ICP could become a valuable tool to investigate novel coil designs since they provide physical insights into optimal coils' shape and geometrical arrangement. Furthermore, they could be used as benchmarks for coil shape optimization algorithms. ⁶⁴

FUNDING INFORMATION

This work was supported in part by NIH R01 EB024536 and was performed under the rubric of the Center for Advanced Imaging Innovation and Research (CAI²R, https://www.cai2r.net), an NIBIB National Center for Biomedical Imaging and Bioengineering (NIH P41 EB017183).

CONFLICT OF INTEREST STATEMENT

Ioannis P. Georgakis was an employee of Corsmed at the time the manuscript was prepared.

ORCID

Ilias I. Giannakopoulos https://orcid.org/0000-0003-2180-5898

Ioannis P. Georgakis https://orcid.org/0000-0002-9672-928X

Daniel K. Sodickson https://orcid.org/0000-0002-2436-4664

Riccardo Lattanzi https://orcid.org/0000-0002-8240-5903

TWITTER

Ilias I. Giannakopoulos IliasGiannakop3

REFERENCES

- 1. Ladd ME, Bachert P, Meyerspeer M, et al. Pros and cons of ultra-high-field MRI/MRS for human application. *Prog Nucl Magn Reson Spectrosc.* 2018;109:1-50.
- 2. Riccardo L, Sodickson DK. Ideal current patterns yielding optimal signal-to-noise ratio and specific absorption rate in magnetic resonance imaging: computational methods and physical insights. *Magn Reson Med.* 2012;68:286-304.
- 3. Georgakis Ioannis P, Polimeridis Athanasios G, Riccardo L. A formalism to investigate the optimal transmit efficiency in radiofrequency shimming. *NMR Biomed*. 2020;33:e4383.
- 4. Lattanzi R, Wiggins GC, Zhang B, Duan Q, Brown R, Sodickson DK. Approaching ultimate intrinsic signal-to-noise ratio with loop and dipole antennas. *Magn Reson Med*. 2018;79:1789-1803.
- Bernhard G, Stockmann JP, Keil B, et al. A 128-channel head coil array for cortical imaging at 7 tesla. Paper presented at: 2021 International Conference on Electromagnetics in Advanced Applications (ICEAA). 2021; Honolulu, HI:367.
- Nader T, Lagore RL, Jungst S, et al. A self-decoupled 32-channel receive array for human-brain MRI at 10.5 T. Magn Reson Med. 2021;86:1759-1772.
- 7. May MW, Hansen SLJD, Mahmutovic M, et al. A patient-friendly 16-channel transmit/64-channel receive coil array for combined head–neck MRI at 7 tesla. *Magn Reson Med*. 2022;88:1419-1433.
- 8. Studios CST Microwave. CST M. CST microwave studio. *CST Studio Suite*. 2008.
- 9. Minana MM. Sim4life: a simulation platform for life sciences and medtech applications. *Eur Cell Mater*. 2014;27:6.
- 10. Fernandez VJ, Polimeridis A, Serralles J. MARIE-a MATLAB-based open source software for the fast electromagnetic analysis of MRI systems. Paper presented at: Proceedings

- of the 23rd Annual Meeting of ISMRM. 2015; Toronto, Canada:709.
- Zoltan C. The development of HFSS. Paper presented at: 2016 USNC-URSI Radio Science Meeting. 2016; Fajardo, PR:39-40.
- 12. Fijany A, Jensen MA, Rahmat-Samii Y, Barhen J. A massively parallel computation strategy for FDTD: time and space parallelism applied to electromagnetics problems. *IEEE Trans Antennas Propagat*. 1995;43:1441-1449.
- Giannakopoulos Ilias I, Litsarev Mikhail S, Polimeridis AG. Memory footprint reduction for the FFT-based volume integral equation method via tensor decompositions. *IEEE Trans Antennas Propagat*. 2019;67:7476-7486.
- Guérin B, Gebhardt M, Serano P, et al. Comparison of simulated parallel transmit body arrays at 3 T using excitation uniformity, global SAR, local SAR, and power efficiency metrics. *Magn Reson Med*. 2015;73:1137-1150.
- 15. Steensma Bart R, Voogt IJ, Kraaij T, et al. Approaching the ultimate intrinsic coil performance for 7T body imaging with high-density parallel transmit/receive arrays. Paper presented at: Proceedings of International Society of Magnetic Resonance in Medicine, Montreal, QC, Canada. 2019:0564.
- Paska J, Raya J, Cloos MA. Fast and intuitive RF-coil optimization pipeline using a mesh-structure. Paper presented at: Proceedings of the ISMRM. 2019; Montréal, QC, Canada:11-16.
- 17. Vaidya MV, Sodickson DK, Collins CM, Lattanzi R. Disentangling the effects of high permittivity materials on signal optimization and sample noise reduction via ideal current patterns. *Magn Reson Med.* 2019;81:2746-2758.
- Sodickson DK, Lattanzi R, Vaidya M, et al. The optimality principle for MR signal excitation and reception: new physical insights into ideal radiofrequency coil design. arXiv preprint arXiv:1808.02087. 2018.
- Avdievich NI, Solomakha G, Ruhm L, Nikulin AV, Magill AW, Scheffler K. Folded-end dipole transceiver array for human whole-brain imaging at 7 T. NMR Biomed. 2021;34: e4541.
- Ertürk MA, Raaijmakers AJE, Adriany G, Uğurbil K, Metzger GJ. A 16-channel combined loop-dipole transceiver array for 7 Tesla body MRI. *Magn Reson Med.* 2017;77:884-894.
- Connell Ian RO, Menon RS. Shape optimization of an electric dipole array for 7 tesla neuroimaging. *IEEE Trans Med Imaging*. 2019;38:2177-2187.
- 22. Raaijmakers AJE, Italiaander M, Voogt IJ, et al. The fractionated dipole antenna: a new antenna for body imaging at 7 Tesla. *Magn Reson Med.* 2016;75:1366-1374.
- 23. Schnell W, Renz W, Vester M, Ermert H. Ultimate signal-to-noise-ratio of surface and body antennas for magnetic resonance imaging. *IEEE Trans Antenna Propagat*. 2000;48:418-428.
- 24. Andreas P, Anke H. The ultimate intrinsic signal-to-noise ratio of loop-and dipole-like current patterns in a realistic human head model. *Magn Reson Med.* 2018;80:2122-2138.
- 25. Polimeridis AG, Villena JF, Daniel L, White JK. Stable FFT-JVIE solvers for fast analysis of highly inhomogeneous dielectric objects. *J Comput Phys.* 2014;269:280-296.
- Guérin B, Villena JF, Polimeridis AG, et al. The ultimate signal-to-noise ratio in realistic body models. *Magn Reson Med*. 2017;78:1969-1980.
- Georgakis IP, Villena JF, Polimeridis AG, Lattanzi R. Novel numerical basis sets for electromagnetic field expansion in

- arbitrary inhomogeneous objects. *IEEE Trans Antenna Propagat*. 2022;70:8227-8241.
- 28. Georgakis Ioannis P, Polimeridis Athanasios G, Riccardo L. Ideal current patterns for optimal SNR in realistic heterogeneous head models. Paper presented at: ISMRM. 2019; Montreal. Canada:1036.
- 29. Harrington RF. The method of moments in electromagnetics. *J Electromagn Wave Appl.* 1987;1:181-200.
- Peter Z, Van Den Berg PM. The three dimensional weak form of the conjugate gradient FFT method for solving scattering problems. *IEEE Trans Microwave Theory Techn.* 1992;40:1757-1766.
- Sancer MI, Sertel K, Volakis JL, VanAlstine P. On volume integral equations. *IEEE Trans Antenna Propagat*. 2006;54:1488-1495.
- 32. Sun LE, Cho CW. A novel formulation of the volume integral equation for electromagnetic scattering. *Waves Random Complex Media*. 2009;19:162-180.
- 33. Yla-Oijala P, Markkanen J, Jarvenpaa S, Kiminki SP. Surface and volume integral equation methods for time-harmonic solutions of Maxwell's equations. *Progr Electromagn Res.* 2014;149:15-44.
- 34. Georgakis IP, Giannakopoulos II, Litsarev MS, Polimeridis AG. A fast volume integral equation solver with linear basis functions for the accurate computation of EM fields in MRI. *IEEE Trans Antenna Propagat*. 2021;69:4020-4032.
- 35. Villena JF, Polimeridis AG, Eryaman Y, et al. Fast electromagnetic analysis of MRI transmit RF coils based on accelerated integral equation methods. *IEEE Trans Biomed Eng.* 2016;63:2250-2261.
- 36. Giannakopoulos Ilias I, Guryev GD, Serralles JE, et al. A hybrid volume-surface integral equation method for rapid electromagnetic simulations in MRI. *IEEE Trans Biomed Eng.* 2022; 70:105-114.
- 37. Lattanzi R, Grant AK, Polimeni JR, et al. Performance evaluation of a 32-element head array with respect to the ultimate intrinsic SNR. *NMR BIOMED*. 2010;23:142-151.
- 38. Khatri C, Radhakrishna RC. Effects of estimated noise covariance matrix in optimal signal detection. *IEEE Trans Acoust Speech Signal Process.* 1987;35:671-679.
- 39. Pruessmann KP, Weiger M, Scheidegger MB, Boesiger P. SENSE: sensitivity encoding for fast MRI. *Magn Reson Med*. 1999;42:952-962.
- Ohliger MA, Grant AK, Sodickson DK. Ultimate intrinsic signal-to-noise ratio for parallel MRI: electromagnetic field considerations. *Magn Reson Med*. 2003;50:1018-1030.
- 41. Ocali O, Atalar E. Ultimate intrinsic signal-to-noise ratio in MRI. *Magn Reson Med.* 1998;39:462-473.
- 42. Balanis CA. *Advanced Engineering Electromagnetics*. John Wiley & Sons; 2012.
- 43. Martini E, Carli G, Maci S. An equivalence theorem based on the use of electric currents radiating in free space. *IEEE Antenna Wirel Propagat Lett.* 2008;7:421-424.
- 44. Giannakopoulos Ilias I, Litsarev Mikhail S, Polimeridis AG. 3D cross-Tucker approximation in FFT-based volume integral equation methods. Paper presented at: 2018 IEEE International Symposium on Antennas and Propagation & USNC/URSI National Radio Science Meeting, Boston, MA. 2018:2507-2508.
- 45. Wiesinger F, Boesiger P, Pruessmann KP. Electrodynamics and ultimate SNR in parallel MR imaging. *Magn Reson Med*. 2004;52:376-390.

- Christ A, Kainz W, Hahn EG, et al. The virtual familydevelopment of surface-based anatomical models of two adults and two children for dosimetric simulations. *Phys Med Biol*. 2010;55:N23-N38.
- 47. Wiggins GC, Triantafyllou C, Potthast A, Reykowski A, Nittka M, Wald LL. 32-channel 3 tesla receive-only phased-array head coil with soccer-ball element geometry. *Magn Reson Med*. 2006;56:216-223.
- Wiggins GC, Polimeni JR, Potthast A, Schmitt M, Alagappan V, Wald LL. 96-channel receive-only head coil for 3 tesla: design optimization and evaluation. *Magn Reson Med*. 2009;62: 754-762.
- 49. Collins Christopher M, Shizhe L, Smith MB. SAR and B1 field distributions in a heterogeneous human head model within a birdcage coil. *Magn Reson Med.* 1998;40:847-856.
- Chen G, Zhang B, Cloos MA, Sodickson DK, Wiggins GC.
 A highly decoupled transmit–receive array design with triangular elements at 7 T. Magn Reson Med. 2018;80: 2267-2274
- 51. Phillips JR, White JK. A precorrected-FFT method for electrostatic analysis of complicated 3-D structures. *IEEE Trans Comput Aid Des Integr Circuit Syst.* 1997;16:1059-1072.
- 52. Saad Y, Schultz MH. GMRES: a generalized minimal residual algorithm for solving nonsymmetric linear systems. *SIAM J Sci Stat Comput.* 1986;7:856-869.
- 53. Giannakopoulos II, Serralles JEC, Daniel L, et al. Magnetic-resonance-based electrical property mapping using global Maxwell tomography with an 8-channel head coil at 7 tesla: a simulation study. *IEEE Trans Biomed Eng.* 2021;68:236-246.
- 54. Rao S, Wilton D, Glisson A. Electromagnetic scattering by surfaces of arbitrary shape. *IEEE Trans Antenna Propagat*. 1982;30:409-418.
- 55. Chai W, Jiao D. Theoretical study on the rank of integral operators for broadband electromagnetic modeling from static to electrodynamic frequencies. *IEEE Trans Compon Packag Manuf Technol.* 2013;3:2113-2126.
- Vaidya MV, Sodickson DK, Lattanzi R. Approaching ultimate intrinsic SNR in a uniform spherical sample with finite arrays of loop coils. Concept Magn Reson Pt B Magn Reson Eng. 2014;44:53-65.
- 57. Kumar A, Bottomley PA. Optimized quadrature surface coil designs. *Magn Reson Mater Phys Biol Med*. 2008;21:41-52.
- Graglia RD, Wilton DR, Peterson AF. Higher order interpolatory vector bases for computational electromagnetics. *IEEE Trans* Antenna Propagat. 1997;45:329-342.
- De Lathauwer L, De Moor B, Vandewalle J. A multilinear singular value decomposition. SIAM J Matrix Anal Appl. 2000;21:1253-1278.
- Giannakopoulos II, Guryev GD, Serrallés JEC, et al. Compression of volume-surface integral equation matrices via Tucker decomposition for magnetic resonance applications. *IEEE Trans Antenna Propagat*. 2022;70:459-471.
- 61. Giannakopoulos Ilias I, Guryev GD, Serralles JE, et al. A tensor train compression scheme for remote volume-surface integral equation interactions. Paper presented at: 2021 International Applied Computational Electromagnetics Society Symposium (ACES). 2021; Hamilton, ON, Canada.
- Oseledets I, Tyrtyshnikov E. TT-cross approximation for multidimensional arrays. *Linear Algebra Appl.* 2010;432:70-88.

- 63. Giannakopoulos Ilias I, Guryev GD, Serralles JE, et al. Decomposition of the incomplete volume-surface integral equation matrices for MR coil simulations. Paper presented at: Proceedings of the 31st Annual Meeting of ISMRM. 2021:1602.
- 64. Cobos Sanchez C, Fernandez Pantoja M, Gomez Martin R. Design of gradient coil for magnetic resonance imaging applying particle-swarm optimization. *IEEE Trans Magn.* 2011;47:4761-4768.

SUPPORTING INFORMATION

Additional supporting information may be found in the online version of the article at the publisher's website.

Figure S1. (left to right) Relative permittivity and electric conductivity for the middle sagittal head section of the numerical human model Duke.

Figure S2. Geometry of the spherical surface which surrounded a homogeneous spherical sample.

Figure S3. Geometry of the surface quadrature array next to the helmet former. The loops were placed outside the helmet former and as close as possible to its surface.

Figure S4. ICP on the spherical shell computed numerically with the proposed approach (top) and analytically using a complete basis of spherical harmonics (bottom) for a voxel located at the center of a homogeneous dielectric sphere for 1:5 T MRI frequency. Both current patterns form two large distributed current loops precessing around the sphere. The first row corresponds to ICP at $\omega t = 0$, while the second row presents them after a $\omega t = \pi/2$ time delay. The spherical sample is omitted from the figure, and instead, the surface shell is shown in gray for visual aid.

Figure S5. ICP on the spherical shell computed numerically with the proposed approach (top) and analytically using a complete basis of spherical harmonics (bottom) for a voxel located at the center of a homogeneous dielectric sphere for 3 T MRI frequency. Both current patterns form two large distributed current loops precessing around the sphere. The first row corresponds to ICP at $\omega t = 0$, while the second row presents them after a $\omega t = \pi/2$ time delay. The spherical sample is omitted from the figure, and instead, the surface shell is shown in gray for visual aid.

Figure S6. Drop of the singular values of $\mathbf{Z}_{cb}^{\mathcal{K}}$ for the four bases.

Figure S7. A temporal snapshot of the ICP yielding optimal SNR at a voxel located in the bottom part of the head for the (A) ultimate, (B) bell, (C) helmet, and (D) cylinder formers at 7 T.

Figure S8. A temporal snapshot of the ICP yielding optimal SNR at a voxel located in the middle of the head for the (A) ultimate, (B) bell, (C) helmet, and (D) cylinder formers at 7 T.

Figure S9. A temporal snapshot of the ICP yielding optimal SNR at a voxel located in the top area of the head for the (A) ultimate, (B) bell, (C) helmet, and (D) cylinder formers at 7 T.

How to cite this article: Giannakopoulos II, Georgakis IP, Sodickson DK, Lattanzi R. Computational methods for the estimation of ideal current patterns in realistic human models. *Magn Reson Med.* 2024;91:760-772. doi: 10.1002/mrm.29864